Electron–phonon interaction in efficient perovskite blue emitters

Xiwen Gong [1], Oleksandr Voznyy [1], Ankit Jain[1], Wenjia Liu[1], Randy Sabatini [1], Zachary Piontkowski[2], Grant Walters[1], Golam Bappi[1], Sergiy Nokhrin[3], Oleksandr Bushuyev[3], Mingjian Yuan[1], Riccardo Comin[1], David McCamant[2], Shana O. Kelley [3,4] and Edward H. Sargent [1*]

Low-dimensional perovskites have—in view of their high radiative recombination rates—shown great promise in achieving high luminescence brightness and colour saturation. Here we investigate the effect of electron–phonon interactions on the luminescence of single crystals of two-dimensional perovskites, showing that reducing these interactions can lead to bright blue emission in two-dimensional perovskites. Resonance Raman spectra and deformation potential analysis show that strong electron–phonon interactions result in fast non-radiative decay, and that this lowers the photoluminescence quantum yield (PLQY). Neutron scattering, solid-state NMR measurements of spin–lattice relaxation, density functional theory simulations and experimental atomic displacement measurements reveal that molecular motion is slowest, and rigidity greatest, in the brightest emitter. By varying the molecular configuration of the ligands, we show that a PLQY up to 79% and linewidth of 20 nm can be reached by controlling crystal rigidity and electron–phonon interactions. Designing crystal structures with electron–phonon interactions in mind offers a previously underexplored avenue to improve optoelectronic materials' performance.

The promise of energy-saving solid-state lighting and full-colour displays has motivated rapid advancements in luminescent materials that exhibit bright emission and high colour purity[1]. Red, green and blue sources that span the full colour gamut are required to generate white light[2]. Blue has proven to be the most challenging[3,4]: in epitaxial inorganic technology, for example, it took 20 additional years to create the first blue light-emitting diodes (LEDs) after red and green LEDs were successfully created in the 1950s and 1960s[5].

A principal challenge for blue emission remains the design of materials that simultaneously exhibit high luminescence efficiency and narrow emission linewidth. Table 1 summarizes the key photophysical properties of currently available blue emitters (Fig. 1e,f). Among inorganic semiconductor single crystals, wide-bandgap analogues of GaAs, GaP, SiC, ZnSe and GaN have been explored[6,7]; however, even the highest-purity and most defect-free epitaxially grown GaN films exhibit a maximum photoluminescence quantum yield (PLQY) of less than 1% at low injection density[8–10]. The loss of luminescence efficiency comes from rapid non-radiative recombination through surface and bulk defects[11], combined with a low radiative recombination rate associated with a small exciton binding energy ($E_b = 20$ meV)[12].

Though inorganic phosphors have demonstrated high brightness with PLQYs over 90%, their relatively insulating nature and long radiative lifetimes result in high turn-on voltages, and this limits their application in LEDs[13,14]. In addition, their spectrally broad luminescence (full width at half maximum, FWHM > 100 nm) diminishes the usable PL yield when a narrow emission bandwidth is required[15]. Similarly, recently synthesized blue organic emitters with 70~85% PLQY in solid-state thin films[16] also suffer from spectrally broad emission (FWHM ~ 75 nm). Organic materials, in contrast to inorganic materials, exhibit binding energies of several

hundred millielectronvolts[17]. Their strongly bound excitons therefore luminesce radiatively with high rates[18], and the desired radiative process dominates recombination (Fig. 1b).

Organic–inorganic hybrid perovskites have emerged as promising candidates for light-emission applications[19]. Chloride-based three-dimensional (3D) perovskites emit in the deep-blue region with sharp emissions (FWHM ~ 25 nm)[20]. However, owing to their small exciton binding energy (~50 meV) and their appreciable trapping losses (Fig. 1c), these materials have so far shown low PLQYs (<1%)[20,21]. Colloidal perovskite quantum dots recently achieved high PLQYs in the blue region through strong quantum confinement[22,23]; however, the high PLQY of colloidal dots has so far been lost once solid-state perovskite CQD films are made[24].

In this work, we focus on reduced-dimensional—also known as 2D layered—perovskites. When we add longer organic ligands to an otherwise 3D perovskite crystal, the new ligands segregate at the surface, and this leads to localization within the newly formed layered materials. Two-dimensional (2D) layered perovskites offer fast radiative recombination rates (k_{rad})[25] due to excitonic localization and therefore are promising candidates to address the above-mentioned need for high PLQY combined with narrow emission width. Photogenerated excitons inside 2D perovskites are strongly confined inside each layer (Fig. 1d). This is exemplified by exciton binding energies that can reach up to 300 meV, values comparable to those of organic materials[26].

Intensive studies have been carried out that have linked structure and performance in low-dimensional (2D, 0D) perovskites[27,28]. The important goal of high luminescence efficiency (PLQY > 80%) with broadband emission (FWHM > 100 nm) has been achieved in the yellow and red regions[29,30]. Nevertheless, blue-emitting perovskites have yet to deliver the desired performance: the PLQY of polycrystalline thin films has been reported to be

[1]Department of Electrical and Computer Engineering, University of Toronto, Toronto, ON, Canada. [2]Department of Chemistry, University of Rochester, Rochester, NY, USA. [3]Department of Chemistry, University of Toronto, Toronto, ON, Canada. [4]Department of Pharmaceutical Sciences, Leslie Dan Faculty of Pharmacy, University of Toronto, Toronto, ON, Canada. *e-mail: ted.sargent@utoronto.ca

Table 1 | Key parameters of deep-blue emitters

| Materials category	Examples	PLQY (%)	Measurement methods	FWHM (nm)	E_b (meV)	k_{rad} (10^7 s^{-1})	References
Inorganic semiconductors	GaN films, nanowires	<1	temperature-dependent PL	20	20	<1	[8–12]
Inorganic phosphors	$KMg_4(PO_4)_3:Eu^{2+}$, $Y_2Mo_4O_{15}:Eu^{3+}$	90	direct measurement in an integration sphere	50	NA	10^{-4}–10^{-1}	[13–15]
Organic solid	$Ir(pmp)_3$	85	NA	80	>200	20	[19]
3D perovskite solid	$CH_3NH_3PbCl_3$ polycrystals	<1	direct measurement in an integration sphere	25	>50	<1	[20,21]
Colloidal perovskite quantum dots	$CsPbX_3$ (X = Br, Cl)	84 (in solution)	comparing with standard dye	32	NA	NA	[22,23]
2D perovskite	$(C_6H_5CH_2NH_3)_2Pb \cdot Br_4$ nanoplates	54 (in solution) 26 (in film)	comparing with standard dye	19	>300	20	[31,33,34]
2D perovskite single crystals	$(C_6H_5CH_2NH_3)_2Pb \cdot Br_4$ exfoliated crystals	79 (best) 60 (average)	Direct measurement in an integration sphere	20	>300	20	this work
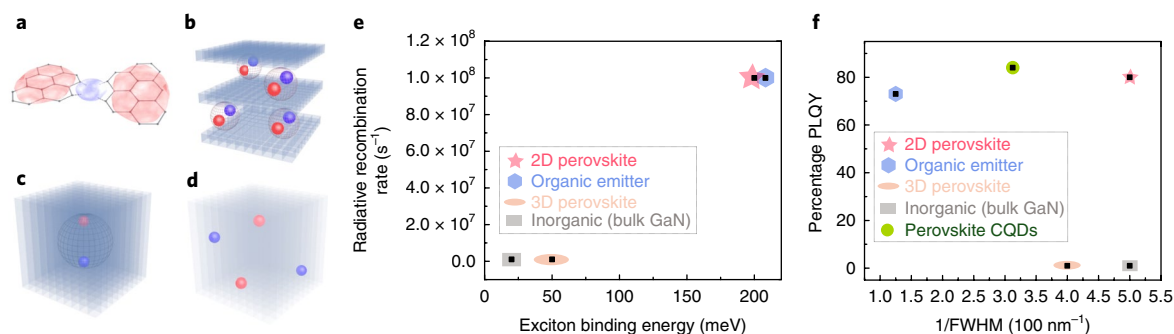
Fig. 1 | Luminescence mechanism of different blue emitters. a, Organic material with strongly confined excitons. **b**, 2D perovskites with bound excitons. **c**, 3D perovskites with weakly bound excitons. **d**, inorganic materials with free carriers. **e**, Radiative recombination rates and exciton binding energies of different emitters. **f**, Comparison of PLQY and the reciprocal of the full width at half maximum of the emission peak between the best 2D single crystal and previously reported blue emitters[9–19]

about 10%, and recently 26% was obtained from atomically thin 2D perovskite single crystals fabricated using a solvent annealing strategy[31–33]. This contrasts with colloidal materials that can achieve high PLQY (54% for 2D perovskites and 84% for 3D perovskite quantum dots[23,34]). The application of 2D perovskites in blue LEDs—which rely on solid-state materials—remains limited by low solid-state PLQYs. We argue herein that the origins of previous low emission efficiencies and large emission linewidths needed further study in order to inform progress towards bright narrowband emitters.

We sought therefore to explore further the potential of 2D perovskite blue emitters using high-quality single crystals, and investigate the determinants of high brightness and thus offer an improved set of guidelines in materials design. Specifically, we focus on the origins of non-radiative rates and on devising strategies to achieve a substantial reduction of these parasitic processes.

In our initial experiments, we sought to produce large (macroscopic, ~mm³ and above) single crystals of 2D perovskite. Single crystals have the potential to achieve high PLQYs due to their low defect densities when compared with polycrystals and amorphous materials; they also provide a platform for studying the determinants of the PLQY of a material, as they are substantially free from the effects of film morphology and grain boundaries. Recent studies have also elucidated the promise of perovskite single crystals directly utilized in electronic device applications[35].

Building these macroscopic, atomically layered sheet structures required us to develop a new synthesis strategy as high-brightness macroscale 2D perovskite single crystals have not previously been reported. We had initially attempted the previously reported vapour diffusion method[36], but the crystals obtained thereby were small in size (<1 mm) and poor in luminescence quality.

Towards the goal of achieving high-quality crystals, we pursued the use of a ternary solvent system to control crystallization kinetics (Fig. S1). Our crystallization strategy was based on a co-solvent N,N-dimethylformamide–dimethylsulfoxide (DMF–DMSO) mixture. When we relied on a mixture of DMF– diethyl ether (DEE) alone, undesirably fast crystallization led to small crystal sizes and low PLQYs. We found that—compared with the case of pure DMF, widely utilized in perovskite preparation—introducing DMSO dramatically enhanced both crystal size and the optical quality of the single crystals. We attribute the improved crystal quality and the high PLQY to the formation of the DMSO–$PbBr_2$ complex[37], which slows the crystallization process, ultimately leading to higher-quality perovskite crystals (Fig. S1 and Table S1). Single crystals grow as DEE slowly diffuses into the perovskite solution[38].

We then explored two classes of organic ammonium cations based either on aliphatic chain group (R = alkyl chain) or phenyl group (Ph = C_6H_5) motifs. The macroscopic shape of the single crystals reveals a strong cation dependence: C4, C12 (R = $CH_3(CH_2)_3$,
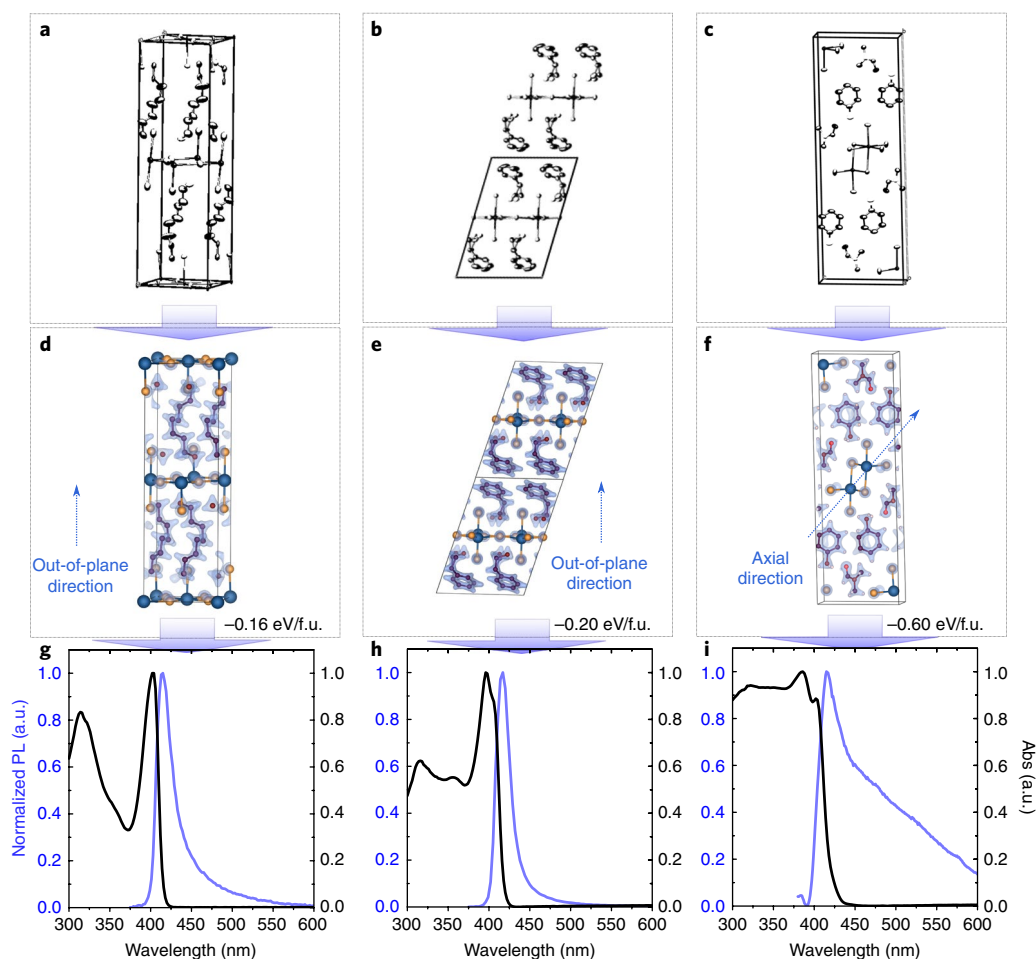
Fig. 2 | Atomic structure and photophysical properties of single-crystal reduced-dimensional blue-emitting perovskites. a–c, Atomic structure of C4, PhC2 and Ph crystals respectively from single-crystal XRD. **d–f**, Simulated total electron charge density of each crystal, using experimental crystal structures. **g–i**, Absorption and PL spectra of crystals. Both C4 and PhC2 among the layered structures show sharp blue emission, wereas Ph emits broadband white light.

$R = CH_3(CH_2)_{11)}$ and PhC, PhC2 (Ph–R = Ph–CH$_2$, Ph–R = Ph–(CH$_2$)$_2$) grow into thin flakes, while with Ph and PhC3 (Ph–R = Ph–(CH$_2$)$_3$) the crystallization results in needle-like crystals (Fig. S2). The products also show dramatically different luminescence properties (Table S2): layer-shaped crystals show narrowband (FWHM ~ 20 nm) deep-blue emission, while needle-shaped crystals result in non-2D crystal structures (Fig. S3) with broadband white-light emissions (Fig. 2g–i, FWHM > 70 nm).

To measure the absolute PLQY, we exfoliated thin samples mechanically from single crystals (Supplementary Materials, Exfoliated sample preparation). Exfoliation reduces the sample thickness and hence the reabsorption of PL (Fig. S4). Crystals that form 2D solids (C4 and PhC2) are easily exfoliated into thin flakes, in contrast with the needle-shaped crystals.

For the deep-blue region, the best sample of PhC2 crystals has a PLQY of 79%, a notable improvement compared with previously reported 2D perovskites[33,34] (Table 1). This high PLQY is also accompanied by a sharp emission spectrum (FWHM ~ 20 nm) and is independent of photoexcitation power (Fig. S5). We account for this by noting the strong excitonic qualities of the 2D perovskites and that no multi-exciton recombination occurs under low injection intensity (10^{10} cm^{-3})[39]. This PLQY is up to two orders of magnitude higher than that of inorganic materials. It is comparable to that of the brightest organic blue emitter (Table 1)[16]; yet, it exhibits

a fully three times narrower emission linewidth (FWHM of 20 nm compared with 75 nm for organic emitters).

We then turned to studying the structure of each crystal with the goal of elucidating the physical origins of the efficient blue emissions. We carried out single-crystal X-ray diffraction (SCXRD) on samples with high PLQY (PhC2), low PLQY (C4) and broadband emission spectra (Ph). In Ph single crystals, the precursors preferentially form a network of truncated PbBr$_6$ octahedra (PbBr$_3$), while plate-shaped crystals (C4 and PhC2) form layered structures, with corner-sharing inorganic PbBr$_6$ octahedra sandwiched between organic layers (Fig. 2d–f). In the PhC2 structure, benzene rings stack between the adjacent PbBr$_6$ layers via CH–π interactions.

To gain further insight into the crystal quality and high PLQY, we carried out density functional theory (DFT) calculations on C4, Ph and PhC2 structures. We first calculated the formation energies of these compounds by relaxing the SCXRD-determined structures. The calculated formation energies of C4, Ph and PhC2 are determined to be 160, 595 and 200 meV/f.u. respectively relative to solid precursors. The higher formation energies suggest more stable structures with a lower chance of defect formation. However, calculations predict Ph to have an indirect bandgap, in contrast with direct bandgaps calculated for C4 and PhC2 (Fig. S6).

We thus focused on the two best 2D perovskites within the aliphatic and phenyl groups (C4 and PhC2 respectively). We carried
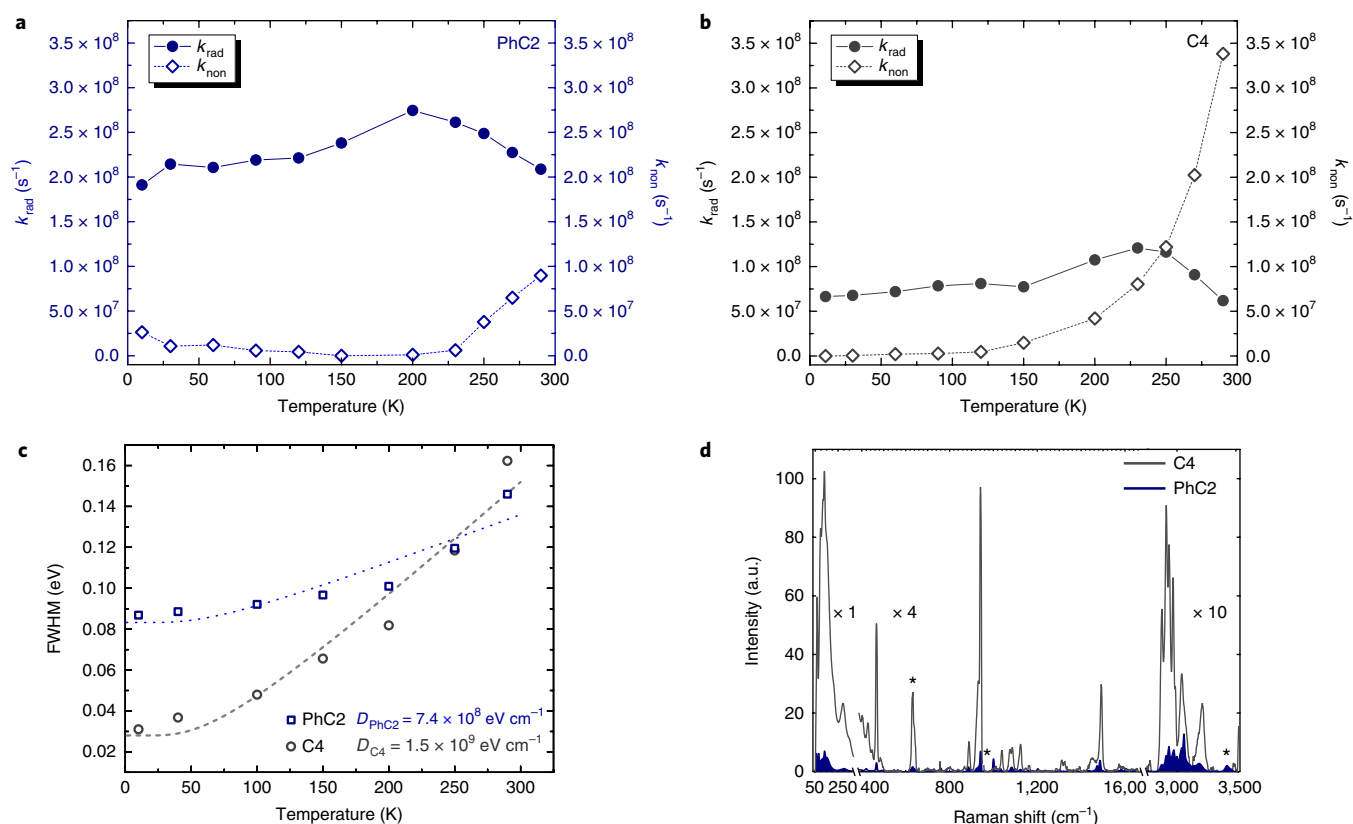
Fig. 3 | Electron–phonon coupling in PhC2 and C4. a,b, Temperature-dependent k_{rad} and k_{non} of PhC2 (**a**) and C4 (**b**) from 10 K to 290 K. **c**, Deformation potential estimation of PhC2 and C4, by fitting the FWHM of the PL profiles at different temperatures. The dotted lines are curves obtained by fitting to the model discussed in the Methods section. **d**, RR spectrum of C4 and PhC2. The asterisks indicate Raman modes associated with the internal standard.

out transient absorption spectroscopy to probe the defect densities in C4 and PhC2 and found comparable densities in these materials, in agreement with DFT calculations (Methods, Fig. S7, S8). The comparable defect densities, contrasted with the dramatic differences in PLQY, led us to probe further the origins of the high brightness for the case of PhC2.

The quantum efficiency is determined by the ratio of the radiative recombination rate (k_{rad}) to the sum of radiative and non-radiative (k_{non}) recombination rates (k_{tot}):

$$\text{PLQY} = \frac{k_{rad}}{k_{tot}} = \frac{k_{rad}}{k_{rad} + k_{non}} \qquad (1)$$

To identify and compare k_{rad} and k_{non}, we used equation (1) with the directly measured k_{tot} (from transient PL) and the measured PLQY (Supplementary Materials, Photoluminescence Measurements, Fig. S9).

Figure 3a shows that radiative recombination is dominant over the entire temperature range for PhC2 crystals, consistent with the fact that their high PLQY is preserved even at room temperature. The fast radiative recombination rate is related to a smaller Bohr radius (Table S3). In the case of C4 crystals, the non-radiative rate surpasses the radiative rate when the temperature increases beyond 250 K (Fig. 3b). The dramatically increased k_{non} results in the pronounced drop of PLQY in C4 to 17% at room temperature. It should be noted that no phase transition was observed over the temperature range discussed here (Fig. S10).

We then investigated the causes of the undesirably rapid k_{non}. From the preceding discussion, we noted that the intrinsic trap densities in C4 and PhC2 are similar, while the k_{non} of C4 is four times

higher than that of PhC2. Clearly the transition from bandedge to trap states must be increased in C4 compared with PhC2. We therefore investigated the role of electron–phonon interactions in facilitating these transitions.

One way to quantify the intensity of electron–phonon interaction is by using the deformation potential (D)—the shift in energy band per unit strain. We extracted D for both PhC2 and C4 by studying the temperature-dependent behaviour of their PL linewidths[40,41] (Table S5). We first observed that the FWHM increases fivefold from 10 K to 290 K in C4, but by less than twofold in PhC2: thermal broadening is dramatically more intense in C4. The quantitative indicator of electron–phonon coupling strength—D—is also twice as high in C4 as in PhC2, reflecting the faster bandedge-to-trap process in the case of C4.

These initial results led us to investigate further the impact of electron–phonon coupling on the electronic transition rate. We selected resonance Raman (RR) spectroscopy since it directly reveals phonon coupling to the electronic transition between the excited and ground states. We employed a photoexcitation energy (457 nm) near the energy of the relevant band-to-band transition. Figure 3d shows the RR spectra of C4 and PhC2 after normalization for sample concentration and transition dipole strength. The C4 RR spectrum is several times more intense than that of PhC2, indicating that the vibrational modes of C4 are substantially more strongly coupled to the electronic excitation than those of PhC2 (Fig. S11, Table S4). C4 is therefore expected to undergo faster non-radiative decay due to the improved vibrational overlap between the ground- and excited-state vibrational wavefunctions. This result corroborates the observed faster k_{non} and lower PLQY for C4 relative to PhC2 (details in Methods).
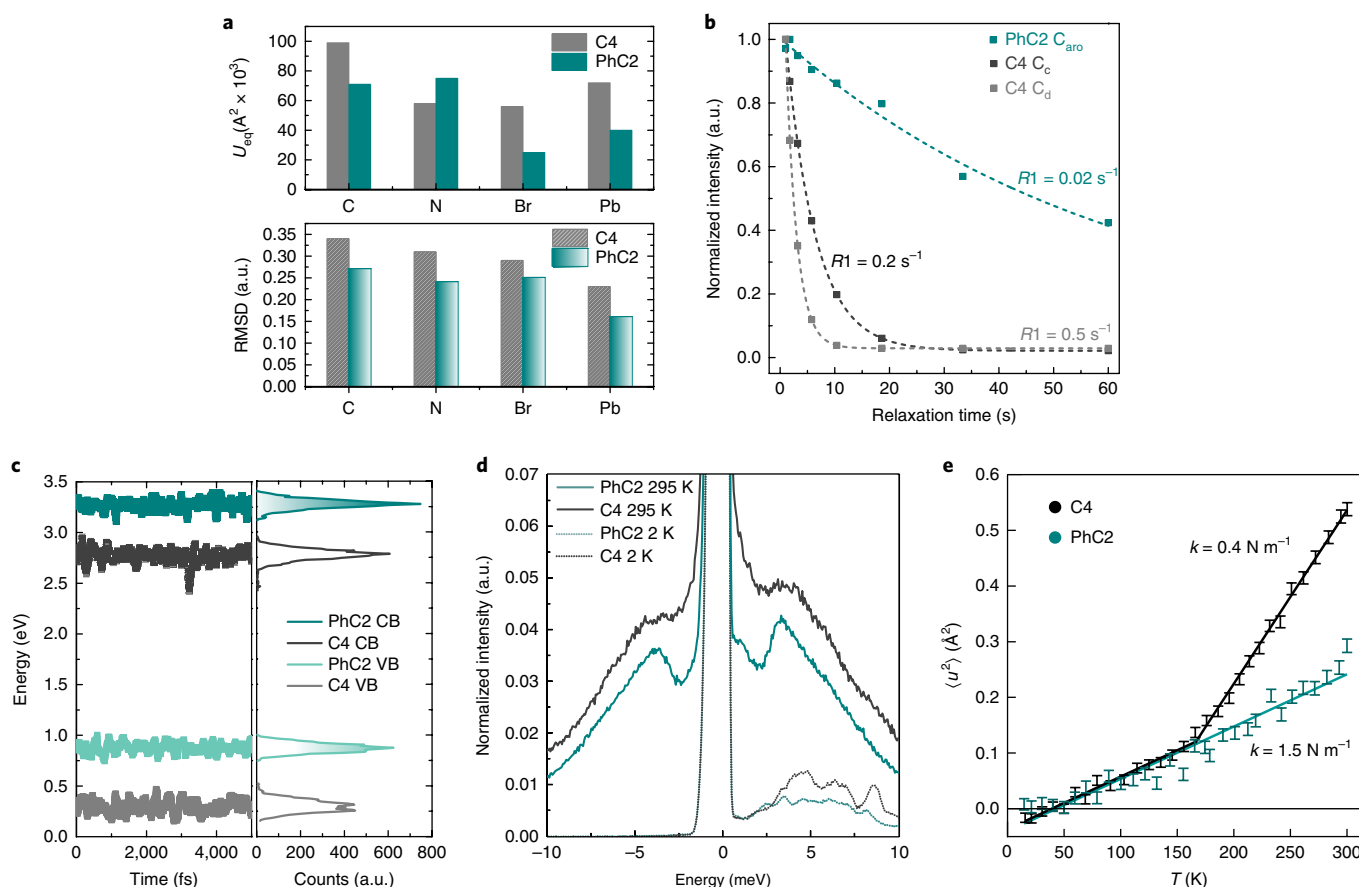
Fig. 4 | Phonon properties of 2D blue emitters. a, Atomic displacement of C, N, Br and Pb of C4 and PhC2 crystals from SCXRD (top) and DFT simulation (panel). **b**, Spin–lattice relaxation rate (R_1) fitting of the terminal aromatic ring carbons of PhC2 crystals and the last two carbon atoms at the methyl terminal of C4 crystals. **c**, Molecular dynamics bandedge fluctuations of C4 and PhC2 (left) and corresponding histogram (right), showing stronger fluctuation in C4. **d**, Neutron scattering spectra of PhC2 and C4 at room temperature and 2 K, with incident neutron energy of 12 meV, $|Q| = 2$–$3\,\text{Å}^{-1}$. Each spectrum was normalized to its elastic scattering peak ($E = 0$ meV). **e**, Mean squared displacement measurements as a function of temperature as determined by elastic neutron scattering. Slopes indicate the mean force constants. Error bars correspond to the statistical error of the linear fit taken between the natural logarithm of the scattering intensity and momentum squared for each temperature that is used to derive the mean squared displacement.

To investigate the connection between material structure and electron–phonon coupling, we characterized the role of crystal rigidity. We sought to compare atomic displacement (from both simulation and experiment), spin–lattice relaxation and the time-variation in the electronic bandstructure.

Atomic displacements—at their essence, optical phonons—are important indicators of crystal rigidity. Figure 4a presents calculation results (bottom panel) alongside experimentally determined atomic displacements for atoms of interest, the latter quantified using the equivalent isotropic displacement parameter (U_{eq}) from single-crystal XRD measurements (Fig. 4a top panel). We find that, in C4, tail carbon atoms have a larger root mean squared displacement compared with respective atoms in PhC2. The larger root mean squared displacement indicates that more phonon modes are activated in C4. In particular, the root mean squared displacements of Br and Pb (which determine the valence band maxima and conduction band minima in perovskites) are higher in the case of C4. Overall, PhC2 shows a more rigid structure.

The crystal rigidity was further investigated using solid-state NMR spin–lattice relaxation time (T_1) measurements (Fig. S12). In the C4 crystal, relaxation rates (R_1) of $0.5\,\text{s}^{-1}$ were observed for terminal methyl carbon (Cd), while PhC2 showed an order of magnitude slower R_1 of $0.02\,\text{s}^{-1}$ at the terminal aromatic ring carbons

(Fig. 4b). This agrees with the observation from SCXRD that the rigid structure of sp^2 phenyl rings results in smaller thermal displacement ellipsoids of atoms and less vibrational motion in PhC2 compared with the case of aliphatic C4. This also agrees with our observation of the sharpened PL emission peak. We propose that denser molecular packing inside the organic layers in the PhC2 structure contributes to higher crystal rigidity.

As noted earlier, the deformation of a crystal results in a change in its crystal geometry and therefore a shift in its electronic energy bandstructure. We can therefore characterize the structural fluctuations by probing the bandstructure. Figure 4c and Fig. S13 present the time variation of the valence band maximum and conduction band minimum in C4, PhC2 and PhC (Fig. S14) from DFT calculations. We plot the histograms of instantaneous bandgaps for each material class. We again see the larger variation in the bandgap in C4 compared with PhC2, consistent with its lower crystal rigidity.

Figure 4d shows the neutron scattering spectra of PhC2 and C4 powders measured at different temperatures. When the temperature is increased from 2 K to room temperature, the low-temperature inelastic features submerge into the broad quasi-elastic scattering peaks, while a pair of damped harmonic oscillator peaks arises. A striking difference can be seen between these peaks for PhC2 and C4; the peaks are considerably narrower in PhC2 than in

C4. This indicates that the ligands of C4 crystals undergo greater librational motions (including the rocking, wagging and twisting modes), while the movement of the lattice in PhC2 is more confined spatially. We ascribe therefore the higher crystal rigidity of PhC2 to the lower conformational freedom of the crystal structure associated with closer packing among the organic molecules.

To further complement these measurements, we measured the mean squared displacement, $\langle u^2 \rangle$, for the crystals. To achieve this, we used elastic neutron scattering as a function of temperature (Fig. 4e). These measurements (which are most sensitive to the motion of hydrogen) give information related to the rigidity possessed by the ligands. The slope of the mean squared displacement with temperature provides a mean force constant that describes the motion of the ligands relative to their equilibrium positions[42]. At low temperatures we see PhC2 and C4 behave similarly, but above about 150 °C the motion of C4 increases, causing it to diverge from PhC2. This behaviour for C4 correlates with the transition to faster k_{non} at higher temperature, as shown in Fig. 3b.

This work reports a deep-blue emitter with a high PLQY based on high-quality 2D perovskite single crystals. The crystal structure and rigidity contribute to achieving the observed brightness and sharp PL spectra. This study elucidates the performance and prospects of high-brightness perovskite emitters towards their potential application in blue light sources.

Methods

Methods, including statements of data availability and any associated accession codes and references, are available at https://doi.org/10.1038/s41563-018-0081-x.

References

1. Forrest, S. R. et al. Highly efficient phosphorescent emission from organic electroluminescent devices. *Nature* **395**, 151–154 (1998).
2. Yang, X., Xu, X. & Zhou, G. Recent advances of the emitters for high performance deep-blue organic light-emitting diodes. *J. Mater. Chem. C. Mater. Opt. Electron. Devices* **3**, 913–944 (2015).
3. Ponce, F. A. & Bour, D. P. Nitride-based semiconductors for blue and green light-emitting devices. *Nature* **386**, 351–359 (1997).
4. Nakamura, S., Pearton, S. & Fasol, G. *The Blue Laser Diode* 1–5 (Springer, Berlin, 2000).
5. Nanishi, Y. Nobel Prize in Physics: the birth of the blue LED. *Nat. Photon.* **8**, 884–886 (2014).
6. Shirasaki, Y., Supran, G. J., Bawendi, M. G. & Bulović, V. Emergence of colloidal quantum-dot light-emitting technologies. *Nat. Photon.* **7**, 933–933 (2013).
7. Gong, X. et al. Highly efficient quantum dot near-infrared light-emitting diodes. *Nat. Photon.* **10**, 253–257 (2016).
8. Reshchikov, M. A. & Korotkov, R. Y. Analysis of the temperature and excitation intensity dependencies of photoluminescence in undoped GaN films. *Phys. Rev. B* **64**, 115205 (2001).
9. Viswanath, A. K., Lee, J. I., Kim, D., Lee, C. R. & Leem, J. Y. Exciton–phonon interactions, exciton binding energy, and their importance in the realization of room-temperature semiconductor lasers based on GaN. *Phys. Rev. B* **58**, 16333–16339 (1998).
10. Reshchikov M. A. & Korotkov R. Y. Analysis of the temperature and excitation intensity dependencies of photoluminescence in undoped GaN films. *Phys. Rev. B* **64**, 115205 (2001).
11. Hauswald, C. et al. Origin of the nonradiative decay of bound excitons in GaN nanowires. *Phys. Rev. B* **90**, 1–9 (2014).
12. Shan, W. et al. Binding energy for the intrinsic excitons in wurtzite GaN. *Phys. Rev. B* **54**, 16369–16372 (1996).
13. Chen, J. et al. Crystal structure and temperature-dependent luminescence characteristics of $KMg_4(PO_4)_3:Eu^{2+}$ phosphor for white light-emitting diodes. *Sci. Rep.* **5**, 9673 (2015).
14. Janulevicius, M. et al. Luminescence and luminescence quenching of highly efficient $Y_2Mo_4O_{15}:Eu^{3+}$ phosphors and ceramics. *Sci. Rep.* **6**, 26098 (2016).
15. George, N. C., Denault, K. A. & Seshadri, R. Phosphors for solid-state white lighting. *Annu. Rev. Mater. Res.* **43**, 481–501 (2013).
16. Lee, J. et al. Deep blue phosphorescent organic light-emitting diodes with very high brightness and efficiency. *Nat. Mater.* **15**, 1–8 (2015).
17. Knupfer, M. Exciton binding energies in organic semiconductors. *Appl. Phys. A* **77**, 623–626 (2003).
18. Christensen, R. L., Drake, R. C. & Phillips, D. Time-resolved fluorescence anisotropy of perylene. *J. Phys. Chem.* **90**, 5960–5967 (1986).
19. Stranks, S. D. & Snaith, H. J. Metal-halide perovskites for photovoltaic and light-emitting devices. *Nat. Nanotech.* **10**, 391–402 (2015).
20. Sargent, E. H. et al. Structural, optical, and electronic studies of wide-bandgap lead halide perovskites. *J. Mater. Chem. C.* **3**, 8839–8843 (2015).
21. Maculan, G. et al. $CH_3NH_3PbCl_3$ single crystals: inverse temperature crystallization and visible-blind UV-photodetector. *J. Phys. Chem. Lett.* **6**, 3781–3786 (2015).
22. Li, J., Gan, L., Fang, Z., He, H. & Ye, Z. Bright tail states in blue-emitting ultrasmall perovskite quantum dots. *J. Phys. Chem. Lett.* **8**, 6002–6008 (2017).
23. Wang, S., Bi, C., Yuan, J., Zhang, L. & Tian, J. Original core–shell structure of cubic $CsPbBr_3$@amorphous $CsPbBr_x$ perovskite quantum dots with a high blue photoluminescence quantum yield of over 80%. *ACS Energy Lett.* **3**, 245–251 (2018).
24. Zhitomirsky, D., Voznyy, O., Hoogland, S. & Sargent, E. H. Measuring charge carrier diffusion in coupled colloidal quantum dot solids. *ACS Nano* **7**, 5282–5290 (2013).
25. Kondo, T. et al. Resonant third-order optical nonlinearity in the layered perovskite-type material $(C_6H_{13}NH_3)_2PbI_4$. *Solid State Commun.* **105**, 503–506 (1998).
26. Saparov, B. & Mitzi, D. B. Organic–inorganic perovskites: structural versatility for functional materials design. *Chem. Rev.* **116**, 4558–4596 (2016).
27. Smith, M. D., Jaffe, A., Dohner, E. R., Lindenberg, A. M. & Karunadasa, H. I. Structural origins of broadband emission from layered Pb–Br hybrid perovskites. *Chem. Sci.* **8**, 4497–4504 (2017).
28. Solis-Ibarra, D., Smith, I. C. & Karunadasa, H. I. Post-synthetic halide conversion and selective halogen capture in hybrid perovskites. *Chem. Sci.* **6**, 4054–4059 (2015).
29. Zhou, C. et al. Highly efficient broadband yellow phosphor based on zero-dimensional tin mixed-halide perovskite. *ACS Appl. Mater. Interfaces* **9**, 44579–44583 (2017).
30. Zhou, C. et al. Luminescent zero-dimensional organic metal halide hybrids with near-unity quantum efficiency. *Z. Chem. Sci.* **9**, 586–593 (2018).
31. Liang, D. et al. Color-pure violet-light-emitting diodes based on layered lead halide perovskite nanoplates. *ACS Nano* **10**, 6897–6904 (2016).
32. Kawano, N. et al. Effects of organic moieties on luminescence properties of organic−inorganic layered perovskite-type compounds. *J. Phys. Chem. C* **118**, 9101–9106 (2014).
33. Dou, L. et al. Atomically thin two-dimensional organic–inorganic hybrid perovskites. *Science* **349**, 1518–1521 (2015).
34. Yuan, Z., Shu, Y., Tian, Y., Xin, Y. & Ma, B. A facile one-pot synthesis of deep blue luminescent lead bromide perovskite microdisks. *Chem. Commun.* **51**, 16385–16388 (2015).
35. Saidaminov, M. I. et al. Planar-integrated single-crystalline perovskite photodetectors. *Nat. Commun.* **6**, 8724 (2015).
36. Müller, P. Practical suggestions for better crystal structures. *Crystallogr. Rev.* **15**, 57–83 (2009).
37. Jeon, N. J. et al. Solvent engineering for high-performance inorganic–organic hybrid perovskite solar cells. *Nat. Mater.* **13**, 897–903 (2014).
38. Shi, D. et al. Low trap-state density and long carrier diffusion in organolead trihalide perovskite single crystals. *Science* **347**, 519–522 (2015).
39. Kitazawa, N. Excitons in two-dimensional layered perovskite compounds: $(C_6H_5C_2H_4NH_3)_2Pb(Br,I)_4$ and $(C_6H_5C_2H_4NH_3)_2Pb(Cl,Br)_4$. *Mater. Sci. Eng. B* **49**, 233–238 (1997).
40. Franceschetti, A., Wei, S.-H. & Zunger, A. Absolute deformation potentials of Al, Si, and NaCl. *Phys. Rev. B* **50**, 17797–17801 (1994).
41. Guo, Z., Wu, X., Zhu, T., Zhu, X. & Huang, L. Electron–phonon scattering in atomically thin 2D perovskites. *ACS Nano* **10**, 9992–9998 (2016).
42. Zaccai, G. How soft is a protein? A protein dynamics force constant measured by neutron scattering. *Science* **288**, 1604–7 (2000).

Author contributions

X.G. and E.H.S. designed and directed this study. X.G. led the experimental work. A.J. and O.V. contributed to DFT simulations. X.G. and W.L. carried out the PLQY

measurements and analysis. Z.P., R.S. and D.M. carried out RR spectroscopy and analysis. R.S. carried out TA measurements. S.N. and O.B. carried out NMR measurement. G.W. carried out the neutron scattering experiments and analysis. M.Y. prepared perovskite precursors. All authors contributed to writing the manuscript.

Competing interests
The authors declare no competing interests.

Additional information
Supplementary information is available for this paper at https://doi.org/10.1038/s41563-018-0081-x.

Reprints and permissions information is available at www.nature.com/reprints.

Correspondence and requests for materials should be addressed to E.H.S.

Publisher's note: Springer Nature remains neutral with regard to jurisdictional claims in published maps and institutional affiliations.

Methods

DFT simulation. Calculations were carried out using a Perdew–Burke–Ernzerhof generalized gradient exchange correlational functional using the projected augmented wave pseudopotentials as implemented in the computational package VASP. All calculations were carried out with planewave basis using a planewave kinetic energy cutoff of 400 eV. The electronic wavevector grids were obtained individually for each material by converging total energies to 0.005 eV/f.u. This corresponds to converged gamma-centred Monkhorst pack electronic wavevector grids of $3 \times 3 \times 1$, $4 \times 4 \times 1$ and $4 \times 4 \times 3$ with 156-, 124- and 188-atom computational cells for C4, Ph and PhC2 respectively. Van der Waals interactions were included in all of our calculations using the DFT-D2 method of Grimme.

Total energy is converged to within 1×10^{-5} eV for each electronic self-consistent loop. We started with experimentally determined crystal structures and carried out structural relaxation until changes in total energy were less than 1×10^{-4} eV.

The formation energies, E_f, were calculated as

$$E_f = \sum E_{prod} - \sum E_{reac}$$

where E_{prod} and E_{reac} are DFT calculated total energies of products and precursors.

Molecular dynamics simulations are carried out within the *NVT* ensemble using the Nose thermostat as implemented in the VASP package. 624- and 752-atom computational cells are used for C4 and PhC2 respectively with a time step of 1 fs. All atoms were initially allowed to equilibrate for 5000 time steps at a temperature of 300 K before the collection of final data.

We obtained the Bohr exciton radius as

$$\epsilon a_0 / m^*$$

where ϵ, a_0 and m^* are the dielectric constant, Bohr radius and exciton effective mass. The dielectric constant used is the macroscopic dielectric constant (including local field effects) as reported by VASP. The Bohr radius is 0.529 Å and m^* is obtained as $m_e m_h / (m_e + m_h)$. m_e and m_h are the electron and hole effective masses obtained by fitting parabolas to bandstructures in the vicinities of the conduction band minimum and valence band maximum respectively.

The simulated atomic displacements are obtained from molecular dynamics simulations at a temperature of 300 K. In particular, molecular dynamics simulations are carried out with a time step of 1 fs. From these molecular dynamics trajectories, average atomic positions are obtained and these average atomic positions are used in the calculations as reference states of instantaneous displacement from the time-dependent trajectories.

Materials and characterization. *Growth of high-quality single crystals.* $PbBr_2$ and ANH_3Br (1 to 2 by molar ratio, 1 M), with A = organic cation, were dissolved in a mixed solvent of DMF and DMSO (Fig. S1). In this study, we found that adding 30–60% DMSO is favourable for high-quality crystal growth, resulting in larger crystal size and PLQY, and this has been utilized as the crystallization condition for all samples. 0.2 ml of perovskite precursor solution was put into a 20 ml vial with no cap, which was put in a larger and sealed container with 40 ml antisolvent (for example, diethyl ether or chloroform). Crystallization proceeds at room temperature and the final products were taken out after few days, rinsed using antisolvent three times and dried under vacuum. All steps were carried out under ambient conditions.

Exfoliated sample preparation. Samples for all PL measurements were prepared by mechanical exfoliation from single crystals. Perovskite single crystals were put on a clear, transparent and non-emissive one-sided tape, on top of which another clean area of tape was folded. Part of the crystal was detached from the crystal for further exfoliation, exposing fresh cleaved layers, and the rest of the crystal remained on the tape. For the PLQY measurements, we chose one piece of crystal and transferred it onto the tape. The lateral dimensions of the chosen crystals are in the macro range of $mm \times mm$, therefore the effect from the grain boundaries is negligible and does not need to be taken into consideration. Samples with reduced thickness and freshly peeled 2D layers were prepared by repeating this process several times. The coverage of crystals on the tape will be multiplied with increasing numbers of exfoliations. The lamp that is utilized as the excitation source for the PLQY measurement has a round spot with a diameter of 2 mm. The tape with various flakes of 2D perovskite crystals was attached to the glass substrate.

Single-crystal X-ray diffraction measurements. Single crystals were mounted on a nylon loop with oil. SCXRD data were collected on a P4 Bruker diffractometer upgraded with a Bruker SMART 1 K CCD (charge-coupled device) detector and a rotating anode utilizing Mo KR radiation ($\lambda = 0.710\,73$ Å). All measurements were made at room temperature. Fitting and refinement of single-crystal structures were done using OLEX2.

The equivalent isotropic displacement parameters (U_{eq} in Fig. 4a, top panel) are defined and quantified as one-third of sum of the eigenvalues of the orthogonalized displacement tensor (U_{ij}). The results come directly from the refinement of the structure from the SCXRD measurement.

Photoluminescence measurements. Absolute PLQY measurements of exfoliated crystals were carried out in a Quanta-Phi integrating sphere. For each measurement, a large perovskite single crystal was ground into small crystals, and crystals with an area of $0.5\,mm \times 0.5\,mm$ and thickness of tens of nanometres were selected for mechanical exfoliation. The exfoliation was continued until the crystals could fully cover the tape and become appropriately thin (around 50 nm). Then the tape was transferred to a clean glass substrate. For each sample, the absorption of the incident pump (350 nm) was controlled between 10% and 15%, so that the film thickness was close enough to make a fair comparison.

The values of PLQY were measured and calculated based on a previously reported method[43]. A continuous-wave xenon excitation lamp was used as the excitation source with an excitation wavelength of 350 nm, with a power density of 0.25–3.5 mW cm^{-2}, and the carrier density was measured around $10^{10} \times cm^{-3}$ (using the following equation $n \cong \frac{\text{incidence power} \times \text{relaxation lifetime} \times \text{absorption coefficient}}{\text{energy of each phonon}}$ with the absorption coefficient approximately $1 \times 10^4\,cm^{-1}$, and about 10^{-9} s). The bandpass values were 5 and 5 nm for the excitation and emission slits, respectively. The incident and PL spectra were collected with the exfoliated sample (tape/exfoliated crystals/glass substrate) directly in the excitation beam path offset from the beam path and removed from the sphere, in accordance with the standard method. The tapes used for exfoliation should not have photoluminescence in the visible range. If the tape absorbs incident light, the effect of the tape should be excluded. For example, 3M Scotch tape absorbs 15% incident light (350 nm excitation) before it reaches the exfoliated crystals, the effect of which was calibrated by multiplying the measured PLQY by $1/(1 - 0.15) = 1.17$. The detector and integrating sphere were calibrated for spectral variance with a Newport white-light source.

Temperature-dependent steady-state PL spectra were collected using an Ocean Optics USB 2000 spectrometer. The sample was in an ARS closed-cycle cryocooler. Time-resolved PL was measured using Horiba TCSPC (time-correlated single-photon counting) components.

I. Temperature-dependent PL (Fig. S8) was plotted by taking the peak intensity of the PL spectra and then normalized to the highest brightness over the temperature range from 10 K to 290 K. At low temperature, $T = 10$ K in this study, the radiative recombination rate is dominant, which leads to PLQYs close to 100% and non-radiative recombination near zero[33]. Therefore, the PLQY at other temperatures can be estimated by the ratio between the PL intensity at high temperature and the low-temperature PL. This method is cross-validated by the current work: the room-temperature PLQYs of PhC2 and C4 are 70% and 17% using this extrapolation approach, which is in good agreement with the independently and directly measured values. In the sample of exfoliated PhC2 single crystals, the PL intensity of PhC2 slightly increased from 10 K to 150 K, which might originate from gradual thermal activation of the bright excitonic state. This is common for nanoscale emitters, where due to the exchange interaction the lowest-energy exciton is always dark (spin forbidden).

II. Temperature-dependent PL dynamics (Fig. 3a,b): we choose the monoexponential decay to obtain the total recombination rate, as exciton decay is a first-order recombination process, and therefore the kinetics follow a monoexponential model. We also observed deviations from monoexponential behaviour mainly after 10 ns (Fig. S8), which we attribute to trap recombination. Therefore, the fitting of the lifetime was mainly done within 10 ns, when PL is the dominant depopulation process of excitons.

III. Power-dependent PLQY measurement (Fig. SX): we vary the incident power density by changing the slit width on the Fluorolog monochromator. The excitation power density was calculated as the measured power divided by the beam area. The power was measured using an Ophir Laser Dual Channel Power Meter, and the beam area was calculated using the given dispersion relations for the monochromator. The PLQY at different powers was measured with the same method as described above.

Resonance Raman spectroscopy. RR spectra of C4 and PhC2 diluted in a KBr pellet were collected with a 457 nm pre-RR pump, from a continuous-wave diode laser (Cobolt). This wavelength was chosen so that the Raman spectra were not contaminated by sample photoluminescence, but it is close enough to electronic resonance that the Raman intensity will be dominated by resonance terms. Scattered light was collected by an aspheric collection lens in a backscattering geometry. The Rayleigh line was attenuated by a 458 nm long-pass edge filter (Semrock, RazorEdge). A single monochromator with a 1200 gr mm^{-1} (600 gr mm^{-1} for the >2700 cm^{-1} region) diffraction grating (Princeton Instruments, TriVista) dispersed the backscattered light onto a CCD camera (Princeton Instruments, Pixis 400). The entrance slit width was kept at 100 μm. Spectra were collected using a 15 s exposure time for 10 accumulations. KBr pellets were prepared to a molar ratio of 0.0051 for C4 (0.5 mmol KBr + 4.4 μmol C4 + 0.36 mmol NaClO4*H$_2$O) and 0.0056 for PhC2 (0.5 mmol KBr + 4.4 umol C4 + 4.9 μmol PhC2 + 0.36 mmol NaClO4*H$_2$O), each with NaClO4*H$_2$O as an internal intensity standard. Raman shift axes were calibrated to phenyl phosphonic acid in a KBr pellet, using frequencies from the Spectral Database of Organic Compounds (SDBS)[44].

The raw spectra were first normalized to the internal intensity standard at 953 cm^{-1} and then scaled for concentration differences. Next, to separate the contributions to the Raman scattering cross-section due to the vibrational Franck–Condon displacements from the strength of the transition dipole, the transition dipole scaling of the signal was taken into account. The spectra were scaled for their relative transition dipole lengths using the experimental rate of radiative decay, since $k_{rad} \propto \mu_{tr}^2$ and $\sigma_{Raman} \propto \mu_{tr}^4$. The radiative decay rates were taken from photoluminescence spectra at 10 K where the quantum efficiency is assumed to be 100%. Since the radiative rate of PhC2 is $(3.6\,ns)^{-1}$ and that of C4 is $(9.5\,ns)^{-1}$, and they emit at the same wavelength,

$$\frac{\mu_{tr}^4(C4)}{\mu_{tr}^4(PhC2)} = \frac{k_{rad}^2(C4)}{k_{rad}^2(PhC2)} = 7.0$$

In other words, a vibrational mode with the same displacement in PhC2 and C4 will have a Raman cross-section that is seven times higher in PhC2 than in C4. In order to isolate a rough measure of the relative displacements between the two perovskites, the C4 Raman spectrum was multiplied by 7.0.

The spectra in Fig. 3d demonstrate that the vibrational modes of C4 are substantially more displaced in the excited state than those of PhC2. This suggests that C4 will have a faster non-radiative decay rate due to the improved vibrational overlap between the ground- and excited-state vibrational wavefunctions. This result corroborates the observed photoluminescence efficiency for C4 relative to PhC2 and suggests that nuclear rigidity upon electronic excitation is an essential feature of efficiently emitting materials. Table S2 contains the Raman shifts and intensities for representative Raman modes of the samples. Fig. S10 represents the control experiments of 457 nm Raman of the ligands in the absence of the perovskite material. From Fig. S10 it is clear that the perovskite structure resonantly enhances the ligand vibrational modes, thus validating the scaling by the relative radiative rates.

Solid-state NMR. A solid-state NMR experiment was carried out on powder samples of C4 and PhC2 on an Agilent DD2 700 MHz NMR spectrometer. Spectra were obtained using a cross-polarization magic angle spinning experiment at 25 °C and 70 °C. The relaxation rates $R_1 = 1/T_1$ were obtained by fitting the intensity of individual ^{13}C resonances as a function of the inversion recovery time τ (details in Supplemental Information). A higher R_1 value indicates higher mobility and faster molecular motion. For the PhC2 sample three peaks were observed, at 128 (phenyl), 43.5 (C$_a$) and 34.8 (C$_b$) ppm, with R_1 relaxation rates of 0.0162 s^{-1} (Ph), 0,1226 s^{-1} (C$_a$) and 0.1135 s^{-1} (C$_b$) at 25 °C and 0.58 s^{-1} (C$_a$) and 0.19 s^{-1} (C$_b$) at 70 °C. For the C4 sample four peaks were observed: 41.38 ppm (C$_a$), 31.25 ppm (C$_b$), 20.47 ppm (C$_c$) and 16.25 ppm (C$_d$) with R_1 relaxation rates of 0.098 s^{-1} (C$_a$), 0.1387 s^{-1} (C$_b$), 0.1828 s^{-1} (C$_c$) and 0.4978 s^{-1} (C$_d$) at 25 °C and 0.7699 s^{-1} (C$_a$), 0.36 s^{-1} (C$_b$), 0.44 s^{-1} (C$_c$) and 0.4982 s^{-1} (C$_d$) at 70 °C.

In C4 crystals, we observed a relaxation rate of 0.5 s^{-1} for the terminal methyl group (C$_d$) compared with 0.1 s^{-1} for the carbon atom proximal to the ammonium group (C$_a$) (Fig. S11), indicating that the terminal methyl group exhibits faster molecular motion. This observation is in good agreement with the increasing thermal ellipsoid size from C$_a$ to C$_d$ from SCXRD data. In comparison, PhC2 shows an R_1 of 0.02 s^{-1} at the aromatic ring end, which is an order of magnitude slower than for the aliphatic carbons (C$_c$, 0.2 s^{-1}; C$_d$, 0.5 s^{-1}).

Transient absorption. Femtosecond pulses were generated using a regeneratively amplified Yb:KGW laser at a 1 kHz repetition rate (Light Conversion, Pharos). A portion of the 1030 nm fundamental was sent through an optical parametric amplifier (Light Conversion, Orpheus), and the second harmonic of the signal pulse was chosen for a 360 nm or 460 nm pump. Both the pump and residual fundamental were sent into an optical bench (Ultrafast, Helios), and the time delay was adjusted by optically delaying the probe pulse, with time steps increasing exponentially. The repetition rate of the pump was halved using an optical chopper. The fundamental was focused into a calcium fluoride crystal to generate a white-light continuum probe, and both the probe and pump were focused onto the sample. The probe was then directed onto a CCD after dispersion by a grating spectrograph (Ultrafast, Helios).

Transient absorption was used to compare the relative number of traps between C4 and PhC2. Exfoliated single-crystal samples were first excited with 360 nm light, with increasing powers ranging from 25 μW to 1000 μW (Fig. S6a,b). For both samples, the magnitude of the bleach signal increases with increasing power, and a negative signal is present at wavelengths longer than 450 nm. Bleaching below the bandgap has been assigned previously to absorption involving trap states within the bandgap[45].

We then photoexcited the same spot on the samples with 460 nm light (Fig. S6c,d), which is only absorbed by trap states (a 450 nm shortpass filter was used to lower the pump scattering). Since this results in electrons in the conduction band, a bleach of the bandgap is still expected. In this way, the observed signal should be proportional to the number of trap states, although we have to ensure that the signal is not influenced by other factors. We measured the transient signal at 500 μW, 1000 μW and 2000 μW pump power, and the observed signal shows a linear dependence on power, ruling out two-photon pumping. In order to exclude effects

from crystal thickness (that is, pathlength) and absorption cross sections, we compared the magnitude of signal obtained from pumping the samples with 1000 μW of 360 nm light (Fig. S7a). C4 has a bleach of about 17 ΔmOD, whereas PhC2 has a signal of about 6 ΔmOD. Essentially, if the two crystals had a similar trap density, we would expect a similar bleach ratio when pumping with 460 nm (Fig. S7b). For clarity, we have included a comparison for 460 nm pumped samples (Fig. S7c), where we have adjusted the spectra to take into account the ratio from the 360 nm pumped experiment (by dividing by a constant equal to the bleach magnitude mentioned above). The resulting spectra (Fig. S7c) show similar bleach magnitudes for C4 and PhC2, with PhC2 even exhibiting a slightly (around 22%) larger signal (that is, number of traps). This indicates that the number of trap states is very unlikely to be the cause behind the difference in PLQY (that is, PLQY of PhC2 is higher than C4).

Deformation potential calculation. The origin of the thermal broadening of exciton emission linewidth stems from the fluctuation of the bandgap, which is caused by the displacement of the atoms in the crystal. Therefore, the temperature dependence of the FWHM is governed by the strength of electron–phonon coupling. One of the quantitative expressions of electron–phonon coupling is the deformation potential (D), defined as the change in the bandgap energy per unit strain due to phonon scattering.

Deformation potential has been used since 1950 to describe the electron–phonon interaction[40]. It is defined as the derivative of the electronic energy levels with respect to strain. One way to estimate deformation potential is by modelling the FWHM of photoluminescence linewidth, the broadening of which is due to phonon scattering when crystal lattice vibrates. We applied the following model to fit the temperature-dependent FWHM of PhC2 and C4 in our study, based on the report from previous literature[41]:

$$FWHM = \Gamma_0 + \frac{\Gamma_{homo}}{e^{\frac{\hbar\omega_{homo}}{k_B T}} - 1}$$

where

$$\Gamma_{homo} = \frac{\hbar M \omega_{homo}}{\rho L}\left(\frac{D}{\hbar\omega_{homo}}\right)^2 \left(2 - e^{-\frac{\hbar\omega_{homo}}{k_B T}}\right)$$

and Γ_0 is the inhomogeneous linewidth due to structure disorder, M is the sum of the electron and hole effective masses, ω_{homo} is the homopolar phonon frequency and D is the deformation potential. At high temperature, Γ_{homo} can be approximated as $\Gamma_{homo} = \frac{\hbar M \omega_{homo}}{\rho L}\left(\frac{D}{\hbar\omega_{homo}}\right)^2$.

In this work, we take the high-temperature approximation and the model can be expressed in the following form:

$$FWHM = \Gamma_0 + \frac{\frac{\hbar M \omega_{homo}}{\rho L}\left(\frac{D}{\hbar\omega_{homo}}\right)^2}{e^{\frac{\hbar\omega_{homo}}{k_B T}} - 1}$$

The effective mass of the electron and hole were calculated using DFT with the results in Table S2; the ω_{homo} homopolar phonon mode for the Pb–Br–Pb stretch was measured from RR results (for PhC2 the corresponding wavenumber is 133 cm^{-1}, and for C4 it is 131 cm^{-1}). Densities (ρ) of for both perovskites are calculated using the unit-cell volume measured from SCXRD (2.8 g cm^{-3} for both materials). The width of the quantum well (L) was quantified using the thickness of the Pb–Br–Pb inorganic layer (0.6 nm).

The fitting results are listed in Table S5.

It also should be noted that the inhomogeneous linewidth (Γ_0) is larger in PhC2 than in C4, indicating that the structural distortion (even at very low temperature) is higher. This structural distortion comes from within the Pb–Br6 octahedra: the Br–Pb–Br bond angle inside the octahedron of PhC2 is 172–174°, instead of the 180° in the C4 crystals. However, structural distortion does not vary with temperature: the Br–Pb–Br bond angle was measured as 168–172° (PhC2) and 180° (C4) at 100 K. The DFT calculations also show that at 0 K the corresponding angle for PhC2 is 168–170° and that for C4 is 180°.

At room temperature, the width of the PL spectra is the combined result of Γ_0 and thermal broadening. We observed that C4 crystals show greater FWHM than PhC2, indicating that the more intense phonon vibration in C4 results in stronger thermal broadening.

Radiative rate calculation. The radiative decay rate k_{rad} of an exciton at $k=0$ in a quantum well structure can be expressed as[46]

$$k_{rad} = \frac{16\,|\mu_{cv}|^2\,\omega_0^2}{\hbar c \omega r_B^2}.$$

μ_{cv} is the transition dipole moment, $\hbar\omega$ is the energy of the exciton and r_B is the Bohr radius of the exciton. From calculation using plain DFT, we calculated the exciton radius of PhC2 and C4 (results in Table S4). Since $r_{B_{PhC2}} = 0.57r_{B_{C4}}$, the radiative rate $k_{rad_{PhC2}} = 3.0k_{rad_{C4}}$.

Neutron scattering. Inelastic neutron scattering measurements were carried out using the Cold Neutron Chopper Spectrometer (CNCS) at the Spallation Neutron Source (SNS), Oak Ridge National Laboratory. An incident neutron beam with an energy of 12 meV and an elastic resolution of 650 μeV was used. Q in this measurement ranges from 0 to 4 Å^{-1}. The perovskite single crystals were ground into powder and then loaded into cylindrical aluminium cans packed under helium for measurement. The spectra were integrated with $|Q| = 2$–3 Å^{-1} and then normalized to the elastic scattering peak ($E = 0$ eV). Background subtraction was done by measuring an empty aluminium can.

Elastic neutron scattering measurements were carried out using the Backscattering Spectrometer (BASIS) at the SNS. Low-statistic scans were performed at 10 K increments. The perovskite single crystals were ground into powder and then loaded into annular aluminium cans packed under helium for measurement. An incident neutron beam with an energy of 2.08 meV was used. Q in this measurement ranges from 0.2 to 2 Å^{-1}.

Data availability. The data that support the plots within this paper and other findings of this study are available from the corresponding author upon reasonable request.

References

43. de Mello, J. C., Wittmann, H. F. & Friend, R. H. An improved experimental determination of external photoluminescence quantum efficiency. *Adv. Mater.* **9**, 230 (1997).
44. Spectral Database of Organic Compounds (SDBS). National Institute of Advanced Industrial Science and Technology. *National Institute of Advanced Industrial Science and Technology* http://www.aist.go.jp/aist_e/latest_research/2004/20041118/20041118.html (2004).
45. Zheng, K. et al. High excitation intensity opens a new trapping channel in organic–inorganic hybrid perovskite nanoparticles. *ACS Energy Lett.* **1**, 1154–1161 (2016).
46. Kawano, N. et al. Effects of organic moieties on luminescence properties of organic–inorganic layered perovskite-type compounds. *J. Phys. Chem. C* **118**, 9101–9106 (2014).